J. Fluid Mech. (2002), *vol.* 462, *pp.* 285–306.
DOI: 10.1017/S0022112002008583 Printed in the United Kingdom

Numerical investigation of the propagation of planar shock waves in saturated flexible porous materials: development of the computer code and comparison with experimental results

By D. LEVI-HEVRONI[1], A. LEVY[1], G. BEN-DOR[1] AND S. SOREK[1,2]

[1]Pearlstone Center for Aeronautical Engineering Studies, Department of Mechanical Engineering, Ben-Gurion University of the Negev, Beer Sheva, Israel

[2]Environmental Hydrology & Microbiology, J. Blaustein Desert Research Institute, Ben-Gurion University of the Negev, Sde Boker Campus, Israel

(Received 23 July 2001 and in revised form 20 December 2001)

The three-dimensional governing equations of the flow field that is developed when an elasto-plastic flexible porous medium, capable of undergoing extremely large deformations, is struck head-on by a shock wave, are developed using a multi-phase approach. The one-dimensional version of these equations is solved numerically using an arbitrary Lagrangian–Eulerian (ALE) based numerical code. The numerical predictions are compared qualitatively to experimental results from various sources and good agreement is obtained. This study complements our earlier study in which we developed and solved, using a total variation diminishing (TVD) based numerical code, the governing equations of the flow field that is developed when an elastic rigid porous medium, capable of undergoing only very small deformations, is struck head-on by a shock wave.

1. Introduction

If a local study of the flow field that is developed inside a porous medium after it is struck head-on by a shock wave is required, an analysis based on a continuum multi-phase approach, rather than a single-phase approach (e.g. the mixing approach), should be carried out.

The basic idea in the single-phase approach is to replace the solid matrix and the fluid occupying the pores by a single fictitious phase. This approach has been applied in two different manners. The first, known as the *bulk approach* is appropriate for both flexible and rigid porous materials.† In this approach, the porous material is assumed to be a single phase whose properties are derived from the properties of the individual phases comprising it. Using this approach, Mazor *et al.* (1994) developed the Lagrangian governing equations describing the head-on collision of planar shock waves with flexible foams. The numerical predictions of this model when compared to experimental results, as reported by Ben-Dor *et al.* (1994), yield relatively good agreement. The second, known as the *pseudo-gas approach*, is appropriate to gas-saturated weak flexible porous materials. In this approach, proposed by Gelfand,

† We use the term 'rigid' in the loose relative sense, which is in common when applied to porous materials, in general, and in particular, i.e. that deformations do not exceed a few percent.

Gubanov & Timofeev (1983), the gaseous phase and the foam matrix are treated as a homogeneous pseudo-gas with new properties. The interaction problem is reduced to the refraction of a planar shock wave at a gaseous interface (i.e. the interface separating the pure gas and the pseudo-gas). Consequently, the flow field can be calculated using gas dynamic relations with the boundary condition that the pressures and the velocities in the flow states on either side of the gas/foam interface are equal. Based on this approach, Gvozdeva & Faresov (1986) and Olim *et al.* (1994) developed an analytical model to calculate various parameters in the flow field.

In the multi-phase approach, the porous medium is considered to be composed of more than one phase, namely the solid matrix and the fluids that occupy its pores, which interact with each other. Baer & Nunziato (1986) present a detailed description of this approach. Baer (1988), Powers, Stewart & Krier (1989) and Levy *et al.* (1993*a*) presented a one-dimensional two-phase analysis with air as the fluid phase. In their numerical solutions, they presented simplified analytical models for calculating the jump conditions across compaction waves in rigid porous materials.

Biot's (1956) analysis referred to microscopic representations of the phase balance equations within the framework of the theory of mixtures and was probably the first to employ the notion of wave propagation in porous media. A large number of papers have appeared in the literature following Biot's pioneering work. Among the recent ones are those by Smeulders, de la Rosette & van Dongen (1992), Degrande & de Roeck (1992) and Nigmatulin & Gubaidulin (1992). Most refer to linear acoustic waves that occur when the momentum dissipation terms dominate. Attenborough (1982), as an example, presented a theory dealing with the motion of sound waves through an ideal saturated porous matrix with parallel cylindrical pores. Using microscopic physical parameters, he extended this theory to account for randomly distributed pores. An extensive literature survey of similar approaches is given by Corapcioglu (1991).

Macroscopic mass, momentum and energy balance equations for the fluid phase and the solid matrix were formulated on the basis of *representative elementary volume* (REV) concepts by Bear & Bachmat (1990). These macroscopic balance equations were composed of averaged flux terms together with integrals of the microscopic exchange flux terms at the phase interfaces. Some unique macroscopic parameters, which emerged from the averaging process, were the tortuosity factor that represents a tensor associated with the matrix directional cosines, the hydraulic radius of the pore spaces, and the porosity that represents the volume fraction of the pores filled by the fluids. Consequently, unlike preceding models (e.g. Baer 1988), which accounted only for the properties of the phases, the macroscopic model developed by Bear & Bachmat (1990) also accounted for the geometrical properties.

Based on these, Bear & Sorek (1990) developed the dominant macroscopic forms of the mass and momentum balance equations following an abrupt pressure impact in saturated porous materials under isothermal conditions. It was shown that during a certain time period, due to the domination of the momentum inertial terms the fluid momentum balance equation conforms to nonlinear waveforms for which the wave speed is also a function of the structure of the porous material.

This initiated the establishment of the macroscopic theoretical basis for wave motion in multi-phase deformable porous media.

Bear *et al.* (1992) and Sorek *et al.* (1992) elaborated these for the case of thermoelastic porous media, describing the theoretical basis for obtaining displacement and shock waves, respectively. Following Sorek *et al.* (1992), Levy *et al.* (1995) introduced additional Forchheimer terms (an additional macroscopic inertial term at the

solid/fluid interface) and obtained a variety of nonlinear wave equation forms. These, together with the development of the evolving balance equations that follow an abrupt simultaneous change of the fluid temperature and pressure, were the major novel theoretical aspects when compared with Nikolaevskij (1990).

Levy *et al.* (1995) conducted a dimensional analysis of these macroscopic balance equations and obtained the macroscopic momentum and energy balance equations, for a saturated (i.e. that all the pores are occupied by the same fluid) elastic rigid (limited to very small deformations) porous medium.

Levy, Ben-Dor & Sorek (1996) developed a total variation diminishing (TVD)-based computer code and numerically solved the full one-dimensional set of governing equations that, as mentioned earlier, was developed and presented by Levy *et al.* (1995). The numerical predictions were compared to experimental results and very good to excellent agreement was evident (see e.g. figures 1 and 2 and subsequent discussion). Many more details can be found in Levy (1995).

Unlike the above-mentioned model of Levy *et al.* (1996), in the present study a model that allows the solid matrix to undergo extremely large deformations is developed. As a result the governing equations include different constitutive equations. In addition, Hooke's law is expressed, in the present case, in terms of the stress rate as a function of the strain rate, i.e. $\dot{\sigma} = f(\dot{\varepsilon})$, rather than the stress as a function of the strain $\sigma = f(\varepsilon)$. This change results in an additional differential equation in the set of governing equations, which, in turn, requires an additional integration. The ability of the porous medium to undergo extremely large deformations prevented us from adopting the TVD-based computer code, which was developed by Levy *et al.* (1996). Instead, a new code, which includes an interface tracking technique, originally proposed by Chan (1975), aimed at tracking the porous medium interface, was developed.

The one-dimensional version of the governing equations is numerically solved. The upwind TVD shock-capturing scheme (which is based on an Eulerian method) originally developed by Harten (1983), is extended to solve the governing equations of the gaseous phase field and a Lagrangian method is extended to solve the governing equations of the solid phase. As a result, a mixed Lagrangian and Eulerian method (ALE) is, in fact, implemented in order to predict the characteristics of the entire flow field.

2. Three-dimensional governing equations

Levy *et al.* (1995) presented a detailed derivation of the three-dimensional macroscopic governing equations describing the flow field that is developed when waves propagate in a saturated porous medium. In the following only the assumptions used in the derivation of the governing equations and the final form of the equations are given.

2.1. *The Assumptions*

(i) The fluid filling the pores is a gas.

(ii) The fluid is ideal, i.e. inviscid, $\mu_f = 0$, and thermally non-conductive, $\lambda_f = 0$. Here μ_f is the dynamic viscosity and λ_f is the thermal conductivity.

(iii) The gas obeys the equation of state of a perfect gas.

(iv) The dispersive and the diffusive mass fluxes of the gaseous phase, and the dispersive flux of the solid phase, are much smaller than the corresponding advective fluxes, and can, therefore, be neglected.

(v) The dispersive momentum fluxes of the gaseous and the solid phases are much smaller than their advective fluxes, and can, therefore, be neglected.

(vi) The conductive and the dispersive heat fluxes of the gaseous phase are negligibly small when compared to their advective heat fluxes.

(vii) The microscopic solid/fluid interfaces are material surfaces with respect to the mass of both the gaseous and the solid phases.

(viii) The solid matrix is flexible, and is assumed to be an elasto-plastic.

(ix) The stress–strain relationships for the solid matrix at the microscopic level and at the macroscopic level have the same form.

(x) The material of which the skeleton of the porous material is made is incompressible.

(xi) The specific heat capacity at constant volume of the fluid, C_f, is constant.

(xii) The energy processes for the gaseous phase are reversible.

(xiii) There are no external energy sources.

(xiv) The energy associated with viscous dissipation is negligibly small.

(xv) The rate of heat transferred between the gaseous and solid phases is negligibly small.

(xvi) The solid phase is isothermal.

2.2. *The balance equations*

The macroscopic mass balance equation for the fluid phase is

$$\frac{\partial}{\partial t}[\phi\rho_g] = -\nabla\cdot[\phi\rho_g \boldsymbol{V}_g], \tag{1}$$

where ρ_g is the density of the fluid, $\boldsymbol{V}_g$ is its velocity vector, and ϕ is the porosity.

The macroscopic mass balance equation for the solid phase is

$$\frac{\partial}{\partial t}[(1-\phi)\rho_s] = -\nabla\cdot[(1-\phi)\rho_s \boldsymbol{V}_s], \tag{2}$$

where ρ_s is the density of the solid (assumed to be constant), and $\boldsymbol{V}_s$ is its velocity vector.

The macroscopic momentum balance equation for the fluid phase is

$$\frac{\partial}{\partial t}(\phi\rho_g \boldsymbol{V}_g) = -\nabla\cdot[\phi\rho_g \boldsymbol{V}_g \boldsymbol{V}_g] - \phi\boldsymbol{T}^*[\nabla P_g + \rho_g g\nabla Z] - \phi\rho_g \tilde{\boldsymbol{F}}_{gs}\boldsymbol{V}_{gs}\boldsymbol{V}_{gs}, \tag{3}$$

where P_g, which denotes the pressure of the fluid, is prescribed by the equation of state (see equation (6)), g denotes the acceleration due to gravity in the Z-direction, $\tilde{\boldsymbol{F}}_{gs}$ and $\boldsymbol{T}^*$ denote the Forchheimer tensor for an isotropic solid matrix and the fluid tortuosity tensor associated with the directional cosines at the solid-fluid interface, and $\boldsymbol{V}_{gs}(\equiv \boldsymbol{V}_g - \boldsymbol{V}_s)$ denotes the relative velocity between the gaseous and solid phases, respectively.

The macroscopic momentum balance equation for the solid phase is

$$\frac{\partial}{\partial t}[(1-\phi)\rho_s \boldsymbol{V}_s] = -\nabla\cdot[(1-\phi)\rho_s \boldsymbol{V}_s \boldsymbol{V}_s] + \nabla\boldsymbol{\sigma}'_s - (1-\phi T^*)\nabla P_g + \phi\rho_g \tilde{\boldsymbol{F}}_{gs}\boldsymbol{V}_{gs}\boldsymbol{V}_{gs} \tag{4}$$

where $\boldsymbol{\sigma}'_s$ denotes the macroscopic constitutive relation for the effective stress of an elasto-plastic solid matrix as given by Bear *et al.* (1992). It is given in equation (7).

The macroscopic energy balance equation for the fluid phase is

$$\frac{\partial}{\partial t}\left[\phi\rho_g\left(\boldsymbol{e}_g+\frac{\boldsymbol{V}_g^2}{2}\right)\right]=-\nabla\cdot\left[\phi\rho_g\boldsymbol{V}_g\left(\boldsymbol{e}_g+\frac{\boldsymbol{V}_g^2}{2}\right)\right]-\phi\boldsymbol{T}^*\boldsymbol{V}_g\nabla P_g$$
$$-\phi\rho_g\tilde{\boldsymbol{F}}_{gs}\boldsymbol{V}_{gs}\boldsymbol{V}_{gs}\boldsymbol{V}_s, \tag{5}$$

where $\boldsymbol{e}_g$ is the internal energy of the fluid.

The equation of state for the fluid phase (i.e. assumed to be a perfect gas) is

$$P_g=\rho_g\Re\,T_g. \tag{6}$$

Here $\Re$ is the specific gas constant and T_g denotes the gas absolute temperature.

It should be noted here that unlike Levy *et al.* (1996), who treated a thermo-elastic solid matrix, an elasto-plastic model is treated in the present model, in order to enable the solid matrix to undergo extremely large deformations. As a result Hooke's law is expressed in terms of the stress rate dependence on the strain rate:

$$\dot{\sigma}'_{si}=\lambda''_s\frac{\dot{V}}{V}+2\mu'_s\dot{\varepsilon}_i \tag{7}$$

where μ'_s and λ''_s are the Lame's constants of a solid, V is the volume of the solid and $\boldsymbol{I}$ denotes a unit tensor. The overdot means a time derivative along a particle path. It should be noted here that natural strain is used when the Hooke's law is expressed in this way. Natural strain means that the strain of an element is referred to the actual configuration instead of the original configuration. The macroscopic strain rate tensor for the solid matrix is defined as

$$\dot{\boldsymbol{\varepsilon}}=\tfrac{1}{2}[\nabla\boldsymbol{V}_s+(\nabla\boldsymbol{V}_s)^T] \tag{8}$$

The volumetric strain can be obtained from the macroscopic mass balance equation. The solid macroscopic mass balance equation along a particle path is

$$\frac{\mathrm{D}}{\mathrm{D}t}[(1-\phi)\rho_s]=-\nabla\cdot\boldsymbol{V}_s. \tag{9}$$

One can define the relative volume, $V=\bar{\rho}_{so}/\bar{\rho}_s$, where $\bar{\rho}_{so}=(1-\phi_o)\rho_s$ and $\bar{\rho}_s=(1-\phi)\rho_s$, and rewrite the mass balance equation in the following form:

$$\frac{1}{V}\frac{\mathrm{D}V}{\mathrm{D}t}=\nabla\cdot\boldsymbol{V}_s. \tag{10}$$

The stresses can be decomposed into a hydrostatic component, $\boldsymbol{P}$, and a deviator component, $\boldsymbol{\tau}$, where P is the mean of the three principle stresses

$$\sigma'_{si}=-P_{si}+\tau_i \tag{11}$$

With the aid of equations (7) and (11) Hooke's law can be expressed as

$$\dot{\tau}_{si}=2\mu'_s\left(\dot{\boldsymbol{\varepsilon}}_i-\frac{1}{3}\frac{\dot{V}}{V}\right),\quad \dot{P}=-K\frac{\dot{V}}{V}, \tag{12}$$

where K, the bulk modulus, is given by $K=(\lambda''_s+2/3\mu'_s)$.

The yield condition (von Mises) is written as

$$\tau_1^2+\tau_2^2+\tau_3^2\leqslant\tfrac{2}{3}(Y^o)^2, \tag{13}$$

where Y^o is the yield strength in simple tension. Following the calculation of the

stress deviators, using Hooke's law (equation (12)), the yield condition, given by equation (13), was checked. If the yield condition was not fulfilled the solid was allowed to deform plastically under a constant stress equal to the maximum value that satisfied equation (13). This was accomplished by multiplying each of the stress deviators by $\sqrt{2/3}\,Y^o/\sqrt{\tau_1^2+\tau_2^2+\tau_3^2}$. The normal stress was independent of the plastic deformation, and an equation of state having the form $P = P(V)$ was used to calculate the normal stress.

2.3. *One-dimensional governing equations*

In the present study, the one-dimensional version of the set of three-dimensional governing equations presented above was solved. The mass, momentum and energy balance equations of the gaseous phase occupying the pores of the porous medium are

$$\frac{\partial}{\partial t}(\phi\rho_g) = -\frac{\partial}{\partial x}(\phi\rho_g u_g), \tag{14}$$

$$\frac{\partial}{\partial t}(\phi\rho_g u_g) = -\frac{\partial}{\partial x}(\phi\rho_g u_g u_g) - \phi T^* \frac{\partial P_g}{\partial x} - \phi\rho_g \tilde{F}_{gs} u_{gs} u_{gs} \tag{15}$$

and

$$\frac{\partial}{\partial t}\left[\phi\rho_g\left(e_g + \frac{u_g^2}{2}\right)\right] = -\frac{\partial}{\partial x}\left[\phi\rho_g u_g\left(e_g + \frac{u_g^2}{2}\right)\right] - T^*\phi u_g \frac{\partial P_g}{\partial x} - \phi\rho_g \tilde{F}_{gs} u_{gs} u_{gs} u_s \tag{16}$$

The conservation of mass and momentum equations of the solid phase along a particle path are

$$\frac{\mathrm{D}\bar{\rho}_s}{\mathrm{D}t} = -\bar{\rho}_s \frac{\partial u_s}{\partial X_s} \tag{17}$$

and

$$\bar{\rho}_s \frac{\mathrm{D}u_s}{\mathrm{D}t} + \frac{\partial \sigma_s'}{\partial X_s} = (1 - \phi T^*)\frac{\partial p_g}{\partial X_s} + \phi\rho_g \tilde{F}_{gs} u_{gs} u_{gs}. \tag{18}$$

3. The numerical method

An upwind TVD shock-capturing scheme, originally developed by Harten (1983), was extended to solve the problem of the gas flow, which described wave propagation and interaction in saturated porous media. Since, in this scheme, it is difficult to keep track of the porous medium interface as it moves through the Eulerian mesh, a mixed Lagrangian and Eulerian method was used in order to keep track of the front and still be able to exchange values from the solution of the gaseous phase with those of the solid phase. The resulting scheme is known as an arbitrary Lagrangian Eulerian (ALE) method. (For more details see Hint, Amsden & Cook 1974.)

3.1. *The TVD scheme for solving the conservation equations of the gaseous phase*

The scheme for solving the conservation equations of the gaseous phase in a conservative form is

$$\boldsymbol{U}_j^{n+1} = \boldsymbol{U}_j^n - \lambda(\bar{\boldsymbol{F}}_{j+1/2} - \bar{\boldsymbol{F}}_{j-1/2}) + \Delta t \boldsymbol{Q}_j, \tag{19}$$

where the parameter λ is defined by

$$\lambda \equiv \Delta t/\Delta x \tag{20}$$

and the numerical flux, $\bar{\boldsymbol{F}}_{j+1/2}$, is evaluated from

$$\bar{\boldsymbol{F}}_{j+1/2} = \frac{1}{2}\left[\boldsymbol{F}(\boldsymbol{U}_j^n) + \boldsymbol{F}(\boldsymbol{U}_{j+1}^n) - \frac{1}{\lambda}\sum_{k=1}^{6}\beta_{j+1/2}^k \boldsymbol{R}_{j+1/2}^k\right], \tag{21}$$

where $\beta_{j+1/2}^k$ is

$$\beta_{j+1/2}^k = \Psi^k(v_{j+1/2}^k + \gamma_{j+1/2}^k)\alpha_{j+1/2}^k - (g_j^k + g_{j+1}^k).$$

The various parameters in the above expression are

$$v_{j+1/2}^k = \lambda a^k(\boldsymbol{U}_{j+1/2}), \tag{22}$$

$$\gamma_{j+1/2}^k = \begin{cases}(g_{i+1}^k - g_i^k)/\alpha_{j+1/2}^k, & \alpha_{j+1/2}^k \neq 0\\ 0, & \alpha_{j+1/2}^k = 0,\end{cases} \tag{23}$$

$$\left.\begin{aligned} g_i^k &= \operatorname{sgn}(\tilde{g}_{j+1/2}^k)\max[0, \min(|\tilde{g}_{j+1/2}^k|, \tilde{g}_{j-1/2}^k \operatorname{sgn}(\tilde{g}_{j+1/2}^k))],\\ \tilde{g}_{j+1/2}^k &= \tfrac{1}{2}[\Psi^k(v_{j+1/2}^k) - (v_{j+1/2}^k)^2]\alpha_{j+1/2}^k,\end{aligned}\right\} \tag{24}$$

$$\Psi(x) = \begin{cases}x^2/4\xi + \xi, & |x| < 2\xi\\ |x|, & |x| \geqslant 2\xi\end{cases}, \qquad \xi = \begin{cases}0.1, & (\partial a^k/\partial \boldsymbol{U})\boldsymbol{R}^k \neq 0\\ 0, & (\partial a^k/\partial \boldsymbol{U})\boldsymbol{R}^k = 0.\end{cases} \tag{25}$$

Based on the conservation equations presented above, $\boldsymbol{U}$, $\boldsymbol{F}$ and $\boldsymbol{Q}$ in (19) are as follows:

$$\boldsymbol{U} = \begin{bmatrix}\bar{\rho}_g\\ m_g\\ E_g\end{bmatrix}, \quad \boldsymbol{F} = \begin{bmatrix}0\\ u_g\bar{\rho}_g + T^*\bar{P}_g\\ u_g(E_g + T^*\bar{P}_g)\end{bmatrix}, \quad Q = \begin{bmatrix}0\\ T^*P\dfrac{\partial\phi}{\partial x} - \tilde{F}\bar{\rho}_g|v_r|v_r\\ u_s\left(T^*P\dfrac{\partial\phi}{\partial x} - \tilde{F}\bar{\rho}_g|v_r|v_r\right)\end{bmatrix}. \tag{26}$$

The macroscopic density and the pressure are $\bar{\rho}_g = \phi\rho_g$ and $\bar{P}_g = \phi P_g$, respectively. The momentum and the energy are $m_g = u_g\bar{\rho}_g$ and $E_g = \bar{\rho}_g(\frac{1}{2}u_g^2 + e_g)$, respectively, and the relative velocity between the gaseous and the solid phases, v_r, is defined as $v_r = u_g - u_s$.

The eigenvalues, a^k, of the Jacobian matrix $A(\boldsymbol{U}) = \partial\boldsymbol{F}/\partial\boldsymbol{U}$ were found symbolically to be

$$a^1 = \hat{u}_g - \hat{c}_g, \quad a^2 = \hat{u}_g, \quad a^3 = \hat{u}_g + \hat{c}_g, \tag{27}$$

where $\hat{u}_g$ and $\hat{c}_g$ are defined in (29).

The corresponding right eigenvectors, $\boldsymbol{R}_k$, were found to be

$$R_1 = \begin{bmatrix}1\\ \hat{u}_g - \hat{c}_g\\ \hat{H}_g - \hat{u}_g\hat{c}_g\end{bmatrix}, \quad R_2 = \begin{bmatrix}1\\ \hat{u}_g\\ \frac{1}{2}\hat{u}_g^2\end{bmatrix}, \quad R_3 = \begin{bmatrix}1\\ \hat{u}_g + \hat{c}_g\\ \hat{H}_g + \hat{u}_g\hat{c}_g\end{bmatrix}. \tag{28}$$

The mean value Jacobian $A(\boldsymbol{U}_L, \boldsymbol{U}_R)$ can be expressed in the form (Roe 1981)

$$\hat{u}_{j+1/2} = \frac{\langle u_g\bar{\rho}_g^{1/2}\rangle}{\bar{\rho}_g^{1/2}}, \quad \hat{H}_{j+1/2} = \frac{\langle H_g\bar{\rho}_g^{1/2}\rangle}{\bar{\rho}_g^{1/2}}, \quad \hat{c}_{j+1/2} = \left\{(\gamma - 1)(\hat{H}_{j+1/2} + \tfrac{1}{2}u_g^2)\right\}^{1/2}, \tag{29}$$

where $\langle b\rangle$ denotes the arithmetic average of the property b, e.g. $\langle b\rangle = \frac{1}{2}(b_j + b_{j+1})$.

The parameters $\alpha^k_{j+1/2}$ were obtained by solving the following linear equation:

$$\boldsymbol{U}_{j+1} - \boldsymbol{U}_j = \sum_{k=1}^{6} \alpha^k_{j+1/2} \boldsymbol{R}^k_{j+1/2},$$

resulting in

$$\left.\begin{aligned} &\alpha_1 = \tfrac{1}{2}(C_1 - C_2), \quad \alpha_2 = \tfrac{1}{2}[\bar{\rho}]C_1, \quad \alpha_3 = \tfrac{1}{2}(C_1 + C_2), \\ &C_1 = \frac{1}{\hat{c}_g^2}(\gamma - 1)\{[E] + \hat{u}_g^2[\bar{\rho}] - u_g[m]\}, \quad C_2 = \frac{1}{\hat{c}_g^2}\{[m] - \hat{u}_g[\bar{\rho}]\} \end{aligned}\right\} \tag{30}$$

where $[b] \equiv b_{i+1} - b_i$, and $\hat{b}$ is the average of the property b within the interval $[x_{i+1} - x_i]$.

3.2. *The Lagrangian scheme for solving the balance equations of the solid phase*

The scheme for solving the balance equations of the solid phase was based on a Lagrangian approach (see Hint *et al.* 1974 and Chan 1975), together with a re-mapping of the solution to the grid of the gaseous phase, in order to calculate the exchange of momentum and energy between the gaseous and the solid phases through the source terms.

The conservation of momentum of the solid phase, in the mass coordinates, is

$$m_s = \int_{X(0,t)}^{X(m,t)} \bar{\rho}_s \, \mathrm{d}V = \int_{X(0,t)}^{X(m,t)} \bar{\rho}_s A \, \mathrm{d}X_s. \tag{31}$$

The conservation of mass for the solid phase is

$$\frac{\mathrm{D}}{\mathrm{D}t}\left(\frac{1}{\bar{\rho}_s}\frac{\partial m_s}{\partial X_s}\right) = 0. \tag{32}$$

Using the mass coordinate, defined in (31), the momentum equation of the solid phase is

$$\frac{\mathrm{D}u_s}{\mathrm{D}t} = \frac{\partial(\boldsymbol{\tau}_s - P_s)}{\partial m_s} - (1 - \phi T^*)\frac{\partial p_v}{\partial m_s} + \frac{1}{\bar{\rho}_s}\tilde{F}_{gs}\phi\rho_g u_{gs}u_{gs}. \tag{33}$$

The deviator component, $\boldsymbol{\tau}$, was calculated from

$$\frac{\mathrm{D}\boldsymbol{\tau}_x}{\mathrm{D}t} = \frac{4}{3}G\dot{\varepsilon}_x = -\frac{4}{3}\frac{\partial u_s}{\partial X} = -\frac{4}{3}G\bar{\rho}_s\frac{\partial u_s}{\partial m_s}. \tag{34}$$

The constitutive equation for the flexible porous material (e.g. foam, which in this study means a highly porous medium, i.e., a material with porosity larger than 0.7) was taken from Zaretsky & Ben-Dor (1996):

$$P_s = \bar{E}_s\eta_{\max}\frac{1}{3}\left[-\ln\left(1 - \frac{\eta}{\eta_{\max}}\right) - B\left(\frac{\eta}{\eta_{\max}}\right)^n\right], \tag{35}$$

where

$$\eta = 1 - \frac{\bar{\rho}_{s0}}{\bar{\rho}_s}, \quad \eta_{\max} = 1 - \frac{\bar{\rho}_{s0}}{\rho_s} = 1 - (1 - \phi) = \phi. \tag{36}$$

The macroscopic Young modulus of the foam as given by Gibson & Ashby (1988) is

$$\bar{E}_s = (1 - \phi)^2 E_s \tag{37}$$

where E_s is the Young modulus of the solid material of which the skeleton of the foam is made.

Based on equation (33), the velocity of the solid phase was calculated by

$$u_j^{n+1/2} = u_j^{n-1/2} - (\boldsymbol{\tau}^n_{j+1/2} - \boldsymbol{\tau}^n_{j-1/2} + P^n_{sj+1/2} - P^n_{sj-1/2} + q^n_{j+1/2} - q^n_{j-1/2})\frac{\Delta t_v}{\Delta m}$$
$$-(1-\phi T^*)^n_j(p^n_{vj+1/2} - p^n_{vj-1/2})\frac{\Delta t_v}{\Delta m} + \frac{\Delta t_v}{\bar{\rho}^n_{sj+1/2}}\tilde{F}_{gs}\phi^n_{j+1/2}\rho^n_{gj+1/2}|u^n_{gsj}|u^n_{sgj}, \quad (38)$$

where the deviator component is

$$\boldsymbol{\tau}^{n+1}_{xj+1/2} = \boldsymbol{\tau}^n_{xj+1/2} - \tfrac{4}{3}G\bar{\rho}^{n+1}_{j+1/2}\frac{u^{n+1/2}_{sj+1} - u^{n+1/2}_{sj-1}}{m_{j+1/2}}. \quad (39)$$

The numerical viscosity in this scheme is given by

$$\left.\begin{aligned} q^{n+1}_{j+1/2} &= \bar{\rho}^{n+1}_{j+1/2}L[aLD - bc^{n+1}_{sj+1/2}]\min(0, D), \\ D &\equiv u^{n+1/2}_{sj+1} - u^{n+1/2}_{sj-1}, \end{aligned}\right\} \quad (40)$$

where a and b are the quadric and linear coefficients of the numerical viscosity, and L is a characteristic length.

The displacement of the solid phase can be obtained by integrating the velocity, i.e.

$$R^{n+1}_{sj} = R^n_{sj} + \Delta t_v u^{n+1/2}_{sj}. \quad (41)$$

The final step was to re-mesh the grid of the solid phase to be compatible with the grid of the gaseous phase. This method is known as the ALE (Arbitrary Lagrangian Eulerian) method (details can be found at Hint *et al.* 1974). A first-order method was used to calculate the density and the velocity of the solid phase in the new grid. Once a solution existed both for the gaseous and the solid phases in the same grid, the solution for the following time step was initiated. A splitting technique was used to solve the multi-phase governing equations of the gaseous and the solid phases, which are coupled through the source terms. First, the balance equations of the gaseous phase were solved with the source terms as evaluated using the flow properties at the previous time step. Then, using the same source terms, the balance equations of the solid phase were solved.

4. Validation of the numerical code

The physical model developed above and the ALE-based numerical code were validated by performing the following two studies: (*a*) a quantitative comparison with both the experimental results of Levy *et al.* (1993*b*) and Levy *et al.* (1996) and the TVD-based numerical predictions for the case of the head-on interaction of planar shock waves with elastic rigid porous materials (i.e. small deformations); and (*b*) a qualitative comparison with the ingenious experimental results of Skews, Atkins & Seitz (1993) for the case of the head-on interaction of planar shock waves with elasto-plastic flexible porous materials (i.e. large deformations). It is important to note that unlike case (*a*) for which a quantitative comparison is fully justified since the two-dimensional effects are negligibly small, only a qualitative comparison could be done in case (*b*) in which two-dimensional effects might play a significant role. Furthermore, even the qualitative comparison was justifiable, and hence conducted, only at the front

and rear cross-sections of the porous medium where the two-dimensional effects are negligibly small.

4.1. *Case a: Head-on interaction of shock waves with elastic rigid porous materials*

Levy *et al.* (1996) conducted a detailed investigation of this case. Consequently, the purpose of the results that are presented in the following is only to provide supporting evidence of the validity of the physical model and numerical code developed here.

Figures 1 and 2 present comparisons of predictions based on the physical model and numerical code developed here with both the experimental results and the numerical predictions of Levy *et al.* (1996) for two cases. In the first case, shown in figure 1, the head-on collision of an incident shock wave, of Mach number $M_s = 1.378$, with a 40 mm long sample made of silicon carbide (SiC) which has 10 pores per inch and an average porosity of 0.728 ± 0.016, is shown. Typical results of the experiment and their numerical simulations, for the gas pressure 43 mm ahead of the front edge of the porous sample, are shown in figure 1(*a*). The pressure histories of the gas occupying the pores of the porous material along the shock tube sidewall (23 mm from the shock tube endwall) and at the shock tube endwall are shown in figures 1(*b*) and 1(*c*), respectively.

In the second case, shown in figure 2, the head-on collision of an incident shock wave, of Mach number $M_s = 1.539$, with a 93 mm long sample made of alumina (Al_2O_3) which has 30 pores per inch and an average porosity of 0.814 ± 0.010, is shown. Typical results of the experiment and their numerical simulations, for the gas pressure 30 mm ahead of the front edge of the porous sample, are shown in figure 2(*a*). The pressure histories of the gas occupying the pores of the porous material along the shock tube sidewall (43 mm from the shock tube endwall) and at the shock tube endwall are shown in figures 2(*b*) and 2(*c*), respectively.

It is clearly seen in both figures 1 and 2 that the predictions of the physical model and ALE-based numerical code developed here are very similar to those of Levy *et al.*'s (1996) TVD-based numerical code. Furthermore, the numerical predictions of both codes reproduce very well the experimentally measured pressure profiles for both the silicon carbide and the alumina foams. Consequently, it could be concluded that our physical model and ALE-based numerical code are valid for the head-on interaction of shock waves with rigid porous materials.

4.2. *Case b: Head-on interaction of shock waves with elasto-plastic flexible porous materials*

Unlike the previous case, the following study and its results are novel and have not been published so far. Therefore, prior to presenting the results it is worthwhile to briefly present the state-of-the-art regarding the head-on interaction of shock waves with elasto-plastic flexible porous materials (e.g. polyurethane foams).

A simple refraction-model-based wave diagram, which was accepted as the state of knowledge until the early 1990s, is shown in figure 3. The head-on collision of the incident shock wave, S_i, results in two shock waves: a reflected shock wave, S_r, back into the gas; and a transmitted shock wave, S_t, into the foam. The transmitted shock wave reflects off the shock tube endwall as a shock wave, S_{tr}, and returns to strike the foam/gas interface (foam face), resulting in a shock wave, S_{trt}, transmitted into the gas and a reflected rarefaction wave, R, back into the foam. This rarefaction wave then reflects off the shock tube endwall as a rarefaction wave, R_r, and returns to interact with the foam/gas interface, resulting in a rarefaction wave, R_{rt}, transmitted into the gas and a reflected compression wave, C, back into the foam. Owing to the

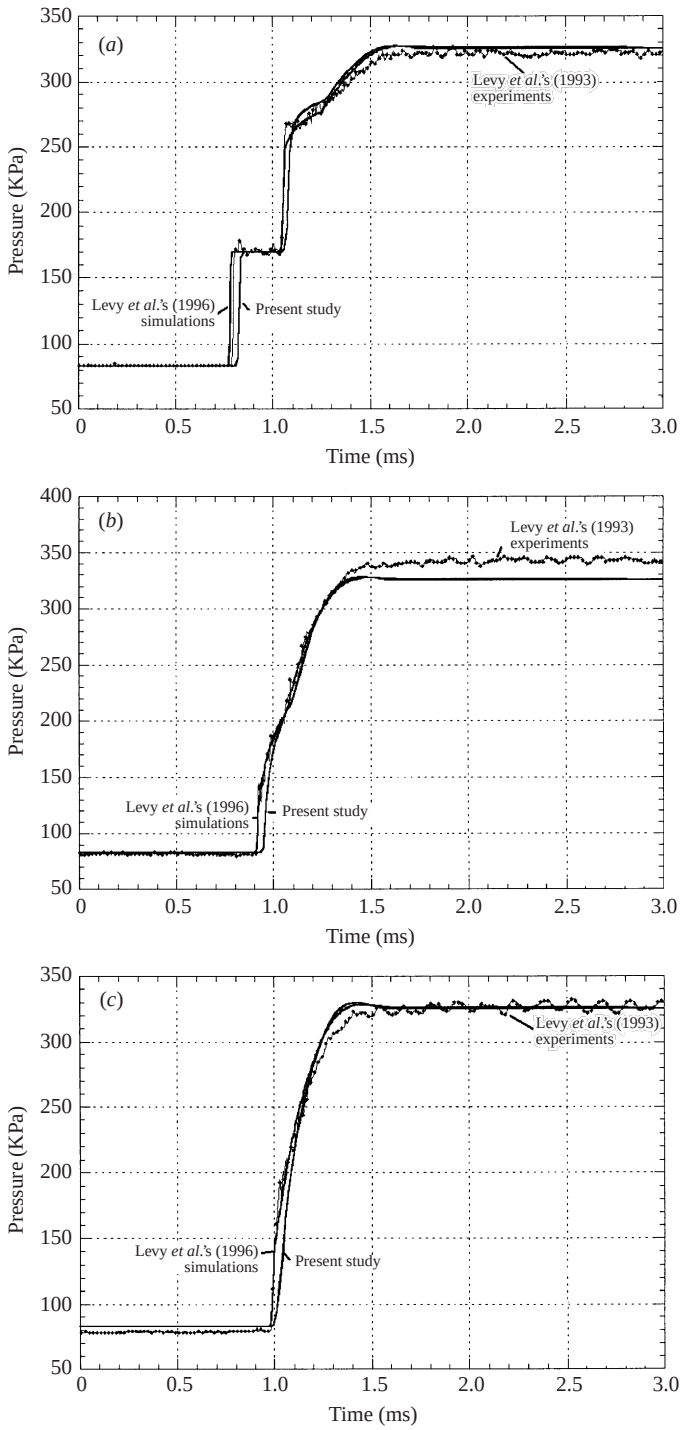

FIGURE 1. Typical experimental results and numerical simulations with a 40 mm long sample made of silicon carbide (SiC) which has 10 pores per inch and average porosity 0.728 ± 0.016. The incident shock wave Mach number in this experiment was $M_s = 1.378$. (*a*) The pressure history of the pure gas 43 mm ahead of the front edge of the porous material. (*b*, *c*) The pressure histories of the gas occupying the pores of the porous material along the shock tube sidewall (23 mm from the endwall) and at its endwall respectively.

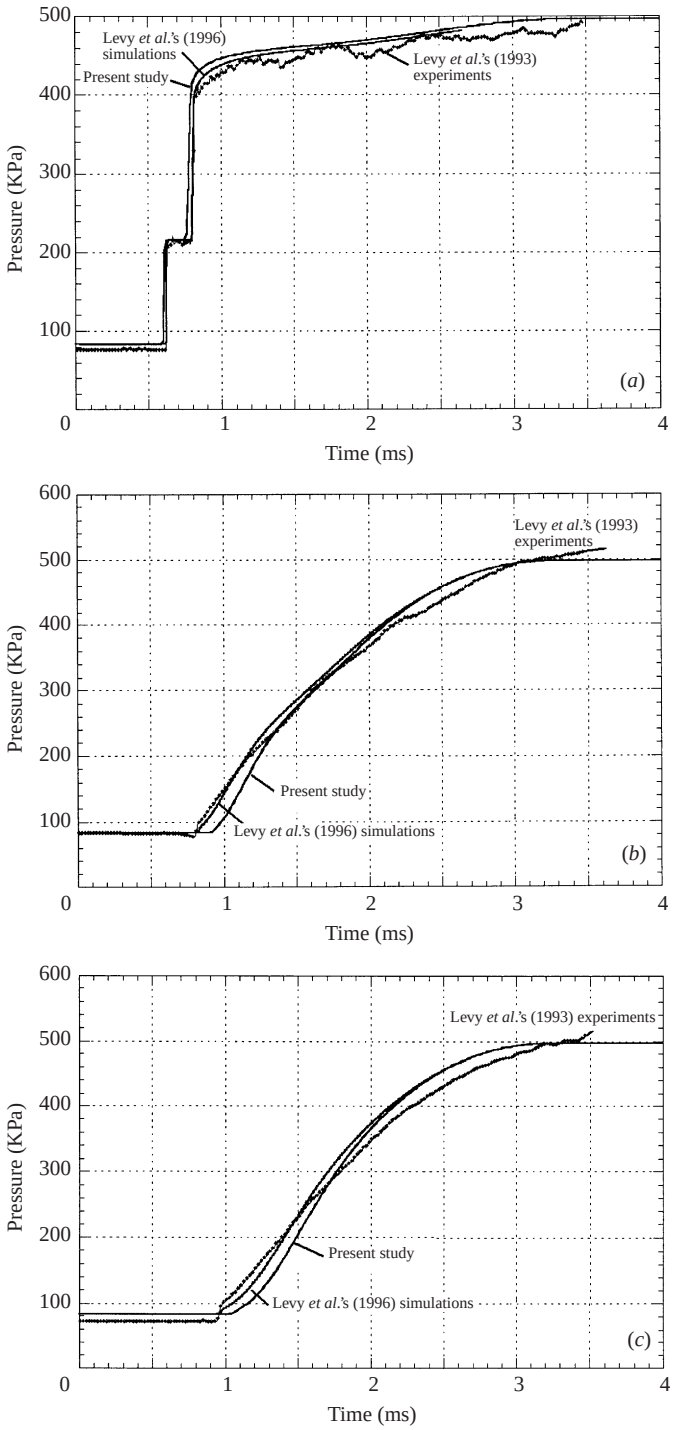

FIGURE 2. Typical experimental results and numerical simulations with a 93 mm long sample made of alumina (Al_2O_3) which has 30 pores per inch and average porosity 0.814 ± 0.01. The incident shock wave Mach number in this experiment was $M_s = 1.539$. (*a*) The pressure histories of the pure gas 30 mm ahead of the front edge of the porous material. (*b*, *c*) The pressure histories of the gas occupying the pores of the porous material along the shock tube sidewall (43 mm from the endwall) and at its endwall respectively.

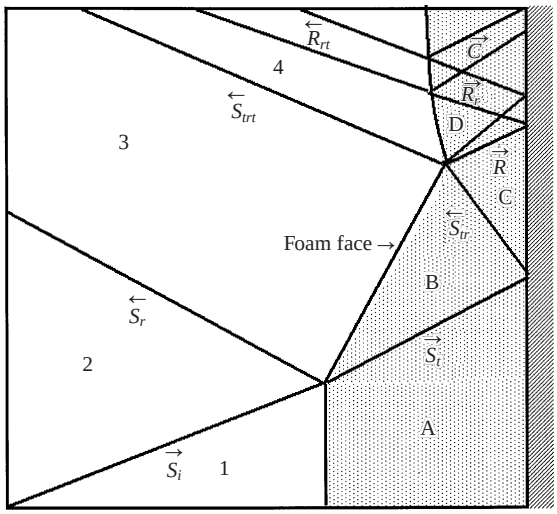

FIGURE 3. A simple refraction-model-based wave diagram of the head-on interaction of a planar shock wave with a flexible porous medium, which was accepted as the state-of-the-art until the early 1990s.

acoustic impedances ratio at the foam/gas interface the reflection from the foam/gas interface of a wave approaching from inside the foam is almost total, i.e. shock and compression waves reflect as rarefaction waves and rarefaction waves reflect as compression waves. When these waves reflect from the shock tube solid endwall they do not change their nature, i.e. rarefaction waves reflect as rarefaction waves and shock/compression waves reflect as shock/compression waves. As a result an almost periodic structure of alternating rarefaction and compression waves that propagate back and forth inside the foam between its front and the shock tube endwall is developed.

Skews *et al.* (1993) discovered, in the course of a comprehensive experimental study, that the wave diagram described above is over simplified since it considers the foam as a single phase while it actually consists of at least two phases (i.e. the solid skeleton and the gas that occupies the pores). Following their experimental study they proposed and forwarded an innovative wave diagram of the interaction, which is shown in figure 4. The incident shock wave, S_i, is seen to collide head-on with the front edge of a 70 mm long foam. As a result of the interaction a shock wave, S_r, is reflected upstream (back into the gas) and two waves, S_{tg} and S_{ts}, are transmitted into the foam; S_{tg} propagates in the gaseous phase that occupies the pores, and S_{ts} propagates in the solid material of which the skeleton of the foam is made. Note that S_{tg} moves faster than S_{ts}. (It should be noted here that for simplicity the back-and-forth bouncing of the alternating compression and rarefaction waves mentioned earlier are not shown in figure 4.) It is also seen in figure 4 that in response to the head-on collision of the shock wave, the foam starts to deform and its front edge (marked 'foam face') follows the two transmitted waves. A deformation of about 75% is seen to take place in the case shown in figure 4. It is also evident that the strong deformation of the foam is followed by a relaxation. In addition, as a result of the very strong deformation the gas, which originally was inside the foam and occupied its pores, crossed the foam/gas interface and emerged out of foam soon after the foam reached its maximum deformation. This is indicated in figure 4 by the contact

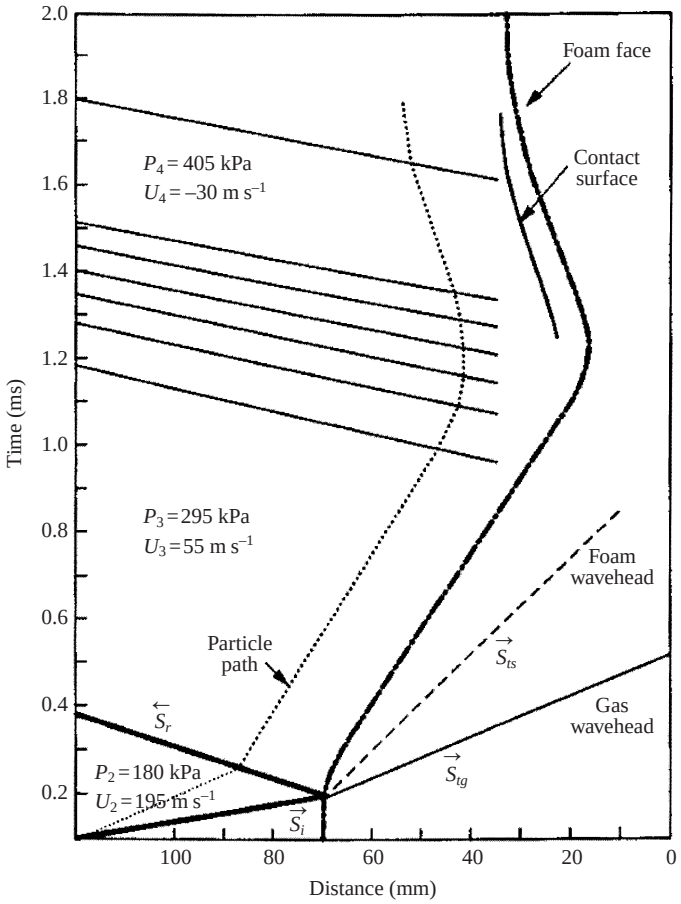

FIGURE 4. An innovative wave diagram of the head-on interaction of a planar shock wave with a flexible porous medium, as proposed by Skews *et al.* (1993) following their comprehensive experimental study, which revealed that the wave diagram shown in figure 3 is over-simplified since it considers the foam as a single phase while it actually consists of at least two phases (i.e. the solid skeleton and the gas that occupies the pores).

surface that separates the gases that were originally outside and inside the foam. Note that in the single-phase model the front edge of the foam is considered as the contact surface, across which the gas cannot flow.

In summary, the two main differences between the over-simplified single-phase (figure 3) and the more realistic two-phase (figure 4) models are the two transmitted waves in the latter case as opposed to the one transmitted wave in the former case, and the emergence of gas from the foam in the latter case.

It is important to note here that the above two-wave diagram models are based on one-dimensional considerations. In a recent study Kitagawa *et al.* (2001) showed that the friction along the shock tube walls and elastic inertia of the porous material introduce two-dimensional effects. Hence, comparisons of one-dimensional calculations with actual experiments are justified only at the front and rear cross-sections of the porous material where two-dimensional effects are negligibly small. For large enough cross-sections or for short enough porous materials the one-dimensional model calculations might also be valid along the centreline. Unfortunately, however, producing

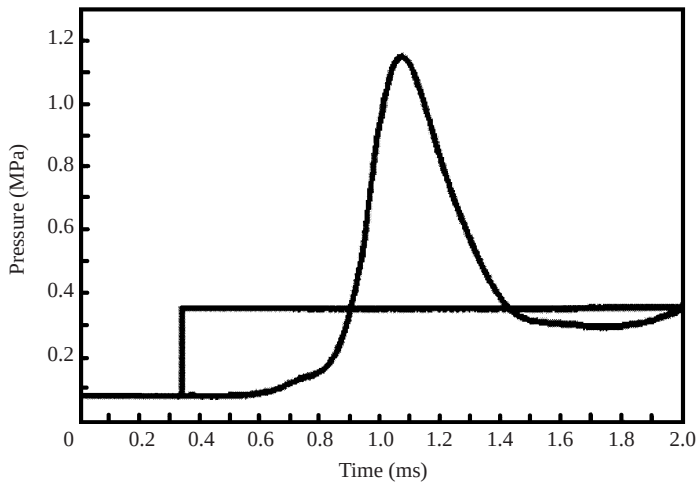

FIGURE 5. The pressure enhancement phenomenon at the shock tube endwall as recorded experimentally by Skews *et al.* (1993). The straight-line stepped trace is the theoretical prediction with no foam present. The pressure behind the head-on reflected shock wave for a rigid wall reflection is constant at about 350 kPa compared to a maximal pressure of about 1150 kPa for the case of a head-on reflection in the presence of the foam.

reliable experimental data along the centreline for polyurethane-type porous media is almost impossible.

Another interesting experimental feature associated with the head-on interaction of shock waves with porous media is the pressure enhancement phenomenon at the shock tube endwall and the dependence of the pressure enhancement on the length of the foam. Gelfand & Gubin (1975) were the first to experimentally show that the presence of the foam results in a higher pressure at the shock tube endwall than for a head-on reflection without foam. The magnitude of the difference was later dealt with by Gelfand *et al.* (1983) and Korobeinikov (1989).

Figure 5 shows this pressure enhancement phenomenon as recorded by Skews *et al.* (1993). The straight-line stepped trace is the theoretical prediction with no foam present. It is evident from figure 5 that the pressure behind the head-on reflected shock wave for a rigid wall reflection is constant at about 350 kPa compared to a maximal pressure of about 1150 kPa for the case of a head-on reflection in the presence of the foam.

Gelfand *et al.* (1983) and Korobeinikov (1989) investigated the dependence of this pressure enhancement phenomenon on the length of the foam. They showed that the shape of the pressure pulse at the shock tube endwall is similar as the length of the foam changes, although the peak pressure increases as the length of the foam increases up to a length beyond which the peak stabilizes and remains at an approximately constant level, depending on the material type and the initial conditions of the experiment. These features are shown in figure 6.

With that background regarding the head-on interaction of shock waves with elasto-plastic flexible porous materials (e.g. polyurethane foams), typical simulation results of the physical model and ALE-based numerical code developed here will be presented. The head-on collision of a shock wave, having a Mach number 1.4, with a polyurethane foam was simulated. The initial pressure and temperature were 100 kPa and 300 K, respectively. The properties of the 120 mm long foam were: material

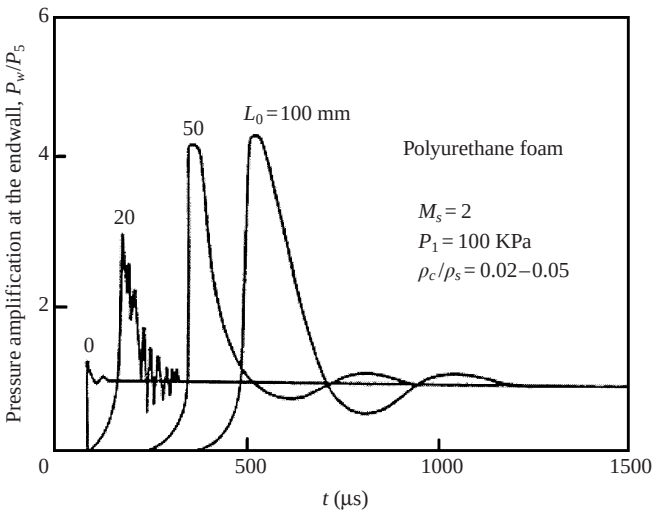

FIGURE 6. The dependence of the pressure enhancement, which was shown in figure 5, on the length of the foam, as recorded experimentally by Gelfand *et al.* (1983) and Korobeinikov (1989).

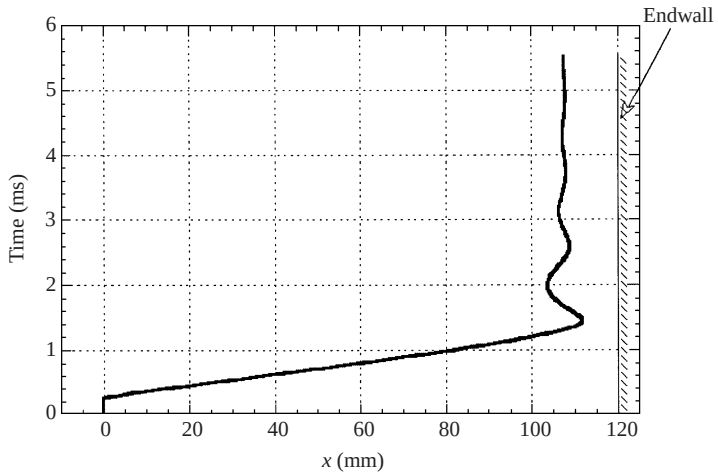

FIGURE 7. The calculated time-dependent trajectory of the foam/gas interface. It is seen, immediately following the head-on collision, to move at a nearly constant velocity, in full agreement with experimental results (see e.g. Ben-Dor *et al.* 1994), until the foam reaches a maximum deformation of about 92%. The constant velocity of the front edge of the foam is about 100 m s^{-1}. This value is close to those measured in similar experiments.

density 1300 kg m^{-3}; porosity 0.98; Poisson ratio 0.45; and Young's modulus 45 MPa. The geometrical coefficients associated with the medium, namely the tortuosity factor and the Forchheimer coefficient, were assumed to be 0.78 and 300 m^{-1}, respectively. An estimation of the values of these coefficients was required since they are not provided in the related literature. For this reason, the comparison between the numerical and the experimental results in the following is only qualitative.

The time-dependence of the trajectory of the foam/gas interface is shown in figure 7. It is seen, immediately following the head-on collision, to move at a nearly constant velocity, in full agreement with experimental results (see e.g. Ben-Dor *et al.* 1994),

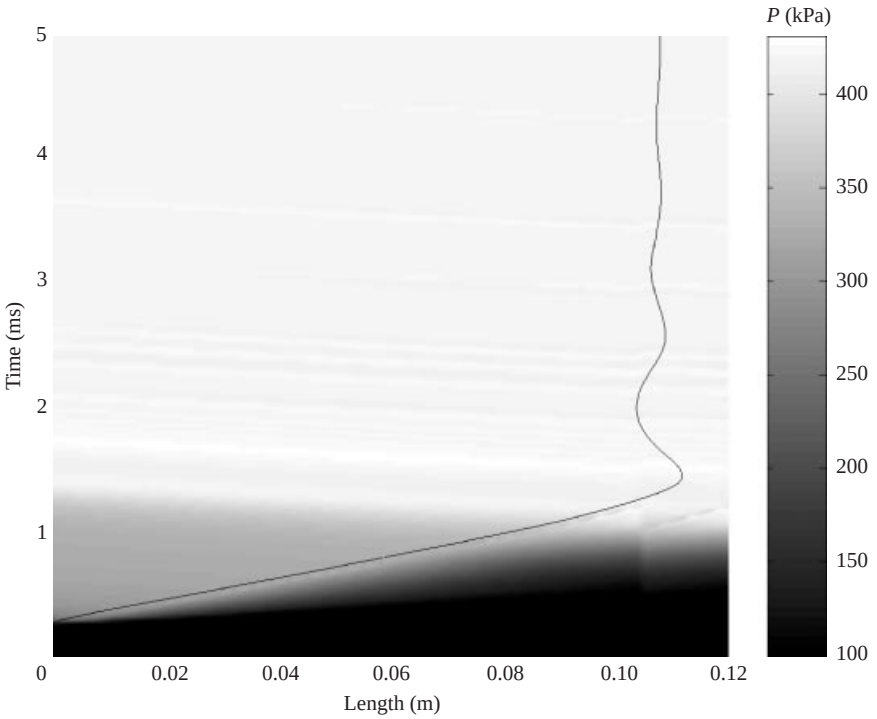

FIGURE 8. A calculated gas pressure map in the (x, t)-plane. The trajectory of the front edge shown in figure 7 is superimposed on this figure. The gas pressure is seen to undulate inside the foam as a result of the periodic structure of alternating rarefaction and compression waves that propagate back and forth inside the foam between its front and back edges. The undulation of the pressure is seen to decay with time. The highest pressure (lightest colour) is obtained behind the shock wave that reflects head-on from the shock tube endwall. (S_{tr} in figure 3). The coupling between the directions of motion of the foam/gas interface and the type of wave that strikes it from inside the foam, i.e. shock/compression (that increases the pressure and induces a velocity in the direction of its propagation) or rarefaction (that decreases the pressure and induces a velocity in the direction opposite to its propagation) is clearly evident.

until the foam reaches a maximum deformation of about 92%. Based on figure 7 the constant velocity of the front edge of the foam is about $100\,\mathrm{m\,s^{-1}}$. This value is close to those measured in similar experiments. At this point the front edge of the foam is seen to undulate back and forth in a decaying manner. This undulation process is a direct result of the periodic structure of alternating rarefaction and compression waves that propagate back and forth inside the foam between its front edge (i.e. the foam/gas interface) and its back edge (i.e. the shock tube endwall).

A calculated gas pressure map in the (x, t)-plane is shown in figure 8. The trajectory of the front edge, which was shown in figure 7, is superimposed on this figure. As a result of the periodic structure of alternating rarefaction and compression waves that propagate back and forth inside the foam between its front and back edges, the gas pressure is also seen to undulate inside the foam. The highest pressure (lightest colour) is obtained behind the shock wave that reflects head-on from the shock tube endwall (S_{tr} in figure 3). As expected the undulation of the pressure decays with time. The coupling between the directions of motion of the foam/gas interface and the type of wave that strikes it from inside the foam, i.e. shock/compression (that increases the pressure and induces a velocity in the direction of its propagation) or rarefaction

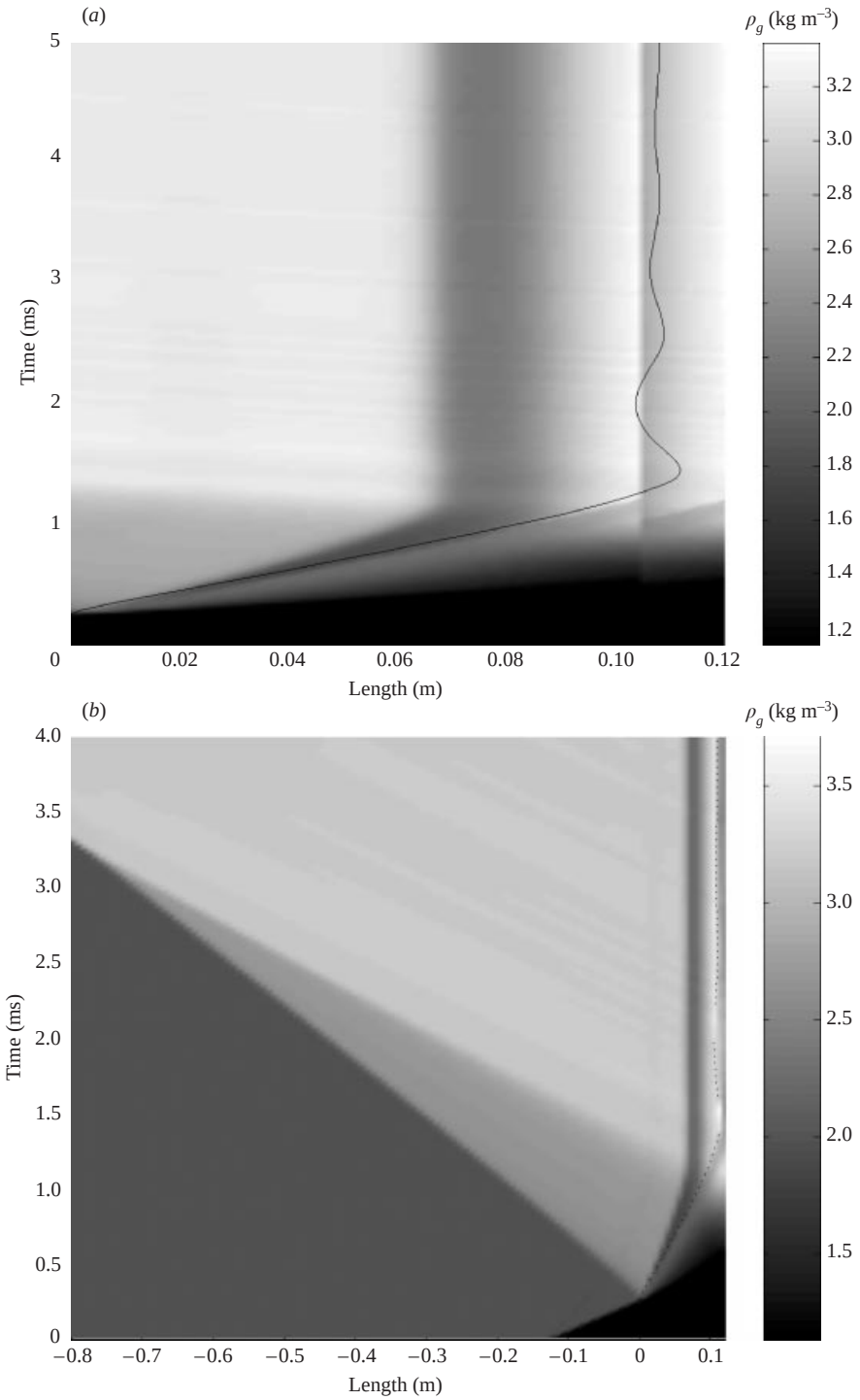

FIGURE 9. For caption see facing page.

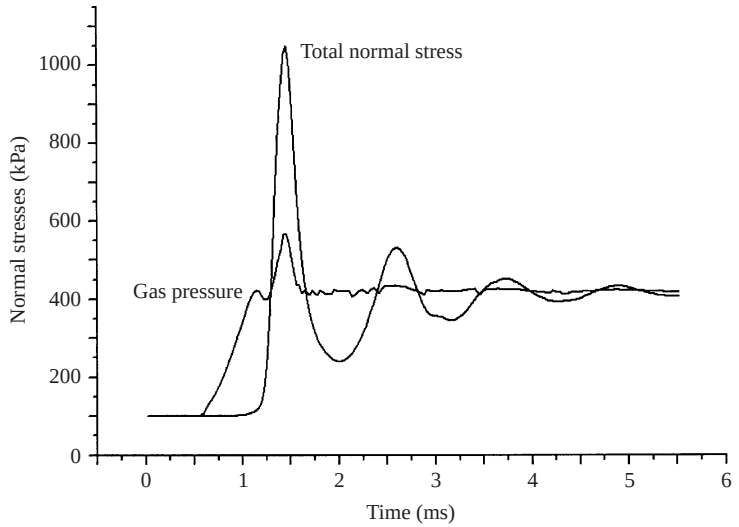

FIGURE 10. The calculated pressure history on the shock tube endwall. The two traces indicate that two waves were transmitted into the foam, i.e. a wave that propagates in the gaseous phase that occupies the pores of the foam (the line labelled as gas pressure), and a wave that propagates in the solid material of which the skeleton of the foam is made (the line labelled as total normal stress). These two waves were labelled in figure 4 as S_{tg} and S_{ts}, respectively. The gas-pressure line shows the gas pressure and the total-normal-stress line shows the overall pressure that is exerted on the shock tube endwall. It is clearly seen that the presence of the foam causes the pressure to increase considerably. An increase from about 410 kPa to about 1050 kPa is seen in the calculation presented. This pressure enhancement is similar to the experimental pressure enhancement results shown in figure 5.

(that decreases the pressure and induces a velocity in the direction opposite to its propagation) is clearly evident in figure 8.

A calculated gas density map in the (x,t)-plane is shown in figure 9(a). The trajectory of the front edge, which was shown in figure 7, is superimposed on this figure too. The contact surface (see figure 4) that, as explained earlier, is a result of the extremely strong deformation that forced the gas, which originally occupied the pores of the foam, to flow across the foam/gas interface and emerge out of the foam soon after it had reached its maximum deformation, is clearly seen in figure 9(a). For comparison the gas density map in the (x,t)-plane is shown in figure 9(b) (on a larger scale) for the case of a head-on collision with a rigid elastic foam, i.e. a foam that undergoes only small deformations. In this case the contact surface that separated the gas that originally occupied the pores of the foam and the gas that entered the foam through the foam/gas interface is clearly seen to be located inside the foam.

The calculated pressure history on the shock tube endwall is shown in figure 10. The two traces are a direct result of the two waves that are transmitted into the foam,

FIGURE 9. Calculated gas density maps in the (x,t)-plane: (a) for a flexible elasto-plastic foam (the trajectory of the front edge shown in figure 7 is superimposed); (b) rigid elastic foam (on a larger scale). The contact surface (see figure 4) that is a result of the extremely strong deformation that forced the gas, which originally occupied the pores of the foam, to flow across the foam/gas interface and emerge from foam soon after it had reached its maximum deformation, is clearly seen in (a). In (b) the contact surface that separated the gas that originally occupied the pores of the foam and the gas that entered the foam through the foam/gas interface is clearly seen to be located inside the foam.

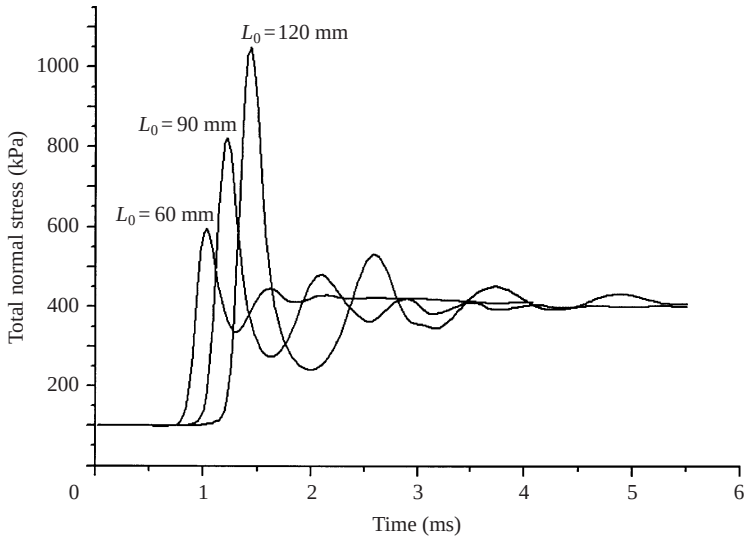

FIGURE 11. The dependence of the pressure enhancement on the length of the foam. The peak pressure increases as the length of the foam increases while the shape of the pressure pulse at the shock tube endwall remains similar. This behaviour is in full agreement with the available experimental results (see e.g. figure 6).

i.e. a wave that propagates in the gaseous phase that occupies the pores of the foam (the line labelled as gas pressure), and a wave that propagates in the solid material of which the skeleton of the foam is made (the line labelled as total normal stress). These two waves were labelled in figure 4 as S_{tg} and S_{ts}, respectively. The gas-pressure line in figure 10 shows the gas pressure and the total-normal-stress line shows the overall pressure that is exerted on the shock tube endwall. The fact that the gas-pressure line starts to rise earlier than the toal-normal-stress line is clear evidence that the wave that propagated in the gaseous phase reached the shock tube endwall before the wave that propagated in the solid material, i.e. S_{tg} moved faster than S_{ts}. It is clearly seen that the presence of the foam causes the pressure to increase considerably. An increase from about 410 kPa to about 1050 kPa is seen in the calculation that is shown in figure 10. This pressure enhancement is similar to the experimental pressure enhancement results that are shown in figure 5.

The dependence of this pressure enhancement on the length of the foam is shown in figure 11. The experimental evidence given above that the peak pressure increases as the length of the foam increases while the shape of the pressure pulse at the shock tube endwall remains similar is clearly seen in figure 11. This behaviour is in full agreement with the available experimental results (see e.g. figure 6).

5. Discussion and conclusions

A physical model and an ALE-based numerical code for calculating the flow field that is formed when a planar shock wave collides head-on with a porous medium have been developed. The model and the code were validated by comparing their predictions with experimental results for two general cases: (*a*) a rigid porous medium that can undergo only very small deformations, and (*b*) a flexible porous medium that can undergo extremely large deformations. While a quantitative comparison was conducted in the first case, only a qualitative comparison was performed in the second

case. Both comparisons revealed good to very good agreement with the experimental results. However, while the former case has already been studied both analytically and numerically (using a TVD-based code) by Levy *et al.* (1996), the latter case has never been, to the best of our knowledge, modelled and successfully solved. Note that unlike the first case, for which a quantitative comparison is fully justified since the two-dimensional effects are negligibly small, only a quantitative comparison could be done in the second case in which two-dimensional effects might play a significant role. Furthermore, even a qualitative comparison was justifiable, and hence performed, only at the front and rear cross-sections of the porous medium where the two-dimensional effects are negligibly small.

The qualitative agreement between the calculations, shown in figures 7 to 11, and the experimental results, shown in figures 3 to 6, clearly indicates that the physical model and numerical code developed here are capable of accurately simulating the head-on collision of a planar shock wave with a flexible foam.

The numerical results successfully illustrated for the first time the following four experimentally observed facts: (*a*) two waves were transmitted into the porous medium as a result of the head-on collision; (*b*) gas emerged out of the porous material soon after the foam reached its maximum deformation; (*c*) the pressure enhancement effect of the foam; and (*d*) the dependence of the pressure enhancement effect on the length of the porous medium.

These successful simulations are the first theoretical and numerical validations of the unique experimental results, which were obtained in the course of the ingenious experimental investigation of Skews *et al.* (1993), that constitute the experimental state-of-the-art regarding the head-on collision of planar shock waves with flexible porous media.

The physical and numerical approaches that were undertaken by us, in the course of this study, can be extended to the case in which the pores of the porous medium are saturated with two fluids rather than one, e.g. a gas and a liquid. This case will be addressed in a future study.

This study was conducted under the auspices of the Dr Morton and Toby Mower Professorial Chair of Shock Wave Studies.

REFERENCES

Attenborough, K. 1982 Acoustical characteristics of porous materials. *Phys. Rep.* **2**, 179–227.

Baer, M. R. 1988 Numerical studies of dynamic compaction of inert and energetic granular materials. *Trans. ASME: J. Appl. Mech.* **55**, 36–43.

Baer, M. R. & Nunziato, J. W. 1986 A two-phase mixture theory for the deflagration to detonation transition (DDT) in reactive granular materials. *Intl J. Multiphase Flow* **12**, 861–889.

Bear, J. & Bachmat, Y. 1990 *Introduction to Modeling of Transport Phenomena in Porous Media.* Kluwer.

Bear, J. & Sorek, S. 1990 Evolution of governing mass and momentum balances following an abrupt pressure impact in porous medium. *Transport in Porous Media* **5**, 169–185.

Bear, J., Sorek, S., Ben-Dor, G. & Mazor, G. 1992 Displacement waves in saturated thermoelastic porous media. I. Basic equations. *Fluid Dyn. Res.* **9**, 155–164.

Ben-Dor, G., Mazor, G., Igra, O., Sorek, S. & Onodera, H. 1994 Shock wave interaction with cellular materials: II. Open cell foams: experimental and numerical results. *Shock Waves* **3**, 167–179.

Biot, M. A. 1956 Theory of propagation of elastic waves in fluid-saturated porous solid. *J. Acoust. Soc. Am.* **28**, 168–191.

Chan, R. K. C. 1975 A generalized arbitrary Lagrangian–Eulerian method for incompressible flows with sharp interfaces. *J. Comput. Phys.* **17**, 311–331.

Corapcioglu, M. Y. 1991 Wave propagation in porous media – a review. In *Transport Processes in Porous Media* (ed. J. Bear & M. Y. Corapcioglu), pp. 373–469. Kluwer.

Degrande, G. & de Roeck, G. 1992 FFT-based spectral analysis methodology for one-dimensional wave propagation in poroelastic media. *Transport in Porous Media* **9**, 85–97.

Gelfand, B. E., Gubanov, A. V. & Timofeev, A. I. 1983 Interaction of shock waves in air with a porous screen. *Isv. Akad. Nauk SSSR, Mekh. Zhid. i Gaza* **4**, 85–92.

Gelfand, B. E. & Gubin, S. A. 1975 Study of special features of propagation and reflection of pressure waves in porous medium. *Sov. Phys. Appl. Math. Tech. Phys.* **6**, 74–77.

Gibson, L. J. & Ashby, M. F. 1988 *Cellular Solids – Structure and Properties*. Program Press, Hill Hall, Oxford, UK.

Gvozdeva, L. G. & Faresov, Yu. M. 1986 Approximate calculation of steady state shock wave parameters in porous compressible materials. *J. Appl. Mech. Tech. Phys.* (English translation of *Zh. Prik. Mekh. Tekh. Fiz.*) **27**, 107–111.

Harten, A. 1983 High resolution schemes for hyperbolic conservation laws. *J. Comput. Phys.* **49**, 357–393.

Hint, C. W., Amsden, A. A. & Cook, J. L. 1974 An arbitrary Lagrangian–Eulerian coupling method for all flow speeds. *J. Comput. Phys.* **14**, 227–253.

Kitagawa, K., Kainuma, N., Ojima, H., Komatsu, M., Takayama, K. & Yasuhara, M. 2001 Visualization of shock wave foam interaction. Presented at *23rd Intl Symp. Shock Waves, Fort Worth, Texas, USA*.

Korobeinikov, V. P. 1989 *Unsteady Interaction of Shock and Detonation Waves in Gases*. Hemisphere.

Levy, A. 1995 Wave propagation in a saturated porous media. PhD thesis, Department of Mechanical Engineering, Ben-Gurion University of the Negev, Beer Sheva, Israel (in Hebrew).

Levy, A., Ben-Dor, G., Skews, B. & Sorek, S. 1993*b* Head-on collision of normal shock waves with rigid porous materials. *Exps. Fluids* **15**, 183–190.

Levy, A., Ben-Dor, G. & Sorek, S. 1996 Numerical investigation of the propagation of shock waves in rigid porous materials: development of the computer code and comparison with experimental results. *J. Fluid Mech.* **324**, 163–179.

Levy, A., Ben-Dor, G., Sorek, S. & Bear, J. 1993*a* Jump conditions across strong compaction waves in gas saturated rigid porous media. *Shock Waves* **3**, 105–111.

Levy, A., Sorek, S., Ben-Dor, G. & Bear, J. 1995 Evolution of the balance equations in saturated thermoelastic porous media following abrupt simultaneous changes in pressure and temperature. *Transport in Porous Media* **21**, 241–268.

Mazor, G., Ben-Dor, G., Igra, O. & Sorek, S. 1994 Shock wave interaction with cellular materials. Part I: Analytical investigation and governing equations. *Shock Waves* **3**, 159–165.

Nigmatulin, R. I. & Gubaidulin, A. A. 1992 Linear waves in saturated porous media. *Transport in Porous Media* **9**, 135–142.

Nikolaevskij, V. M. 1990 *Mechanics of Porous and Fractured Media*. World Scientific.

Olim, M., van Dongen, M. E. W., Kitamura, T. & Takayama, K. 1994 Numerical simulation of the propagation of shock waves in compressible open-cell porous foams. *Intl J. Multiphase Flow* **20**, 557–568.

Powers, J. M., Stewart, D. S. & Krier, H. 1989 Analysis of steady compaction waves in porous materials. *Trans. ASME: J. Appl. Mech.* **56**, 15–24.

Roe, P. L. 1981 Approximate Riemann solvers, parameter vectors and difference schemes. *J. Comput. Phys.* **43**, 357–372.

Skews, B. W., Atkins, M. D. & Seitz, M. W. 1993 The impact of shock waves on porous compressible foams. *J. Fluid Mech.* **253**, 245–265.

Smeulders, D. M. J., de La Rosette, S. P. M. & van Dongen, M. E. H. 1992 Waves in partially saturated porous media. *Transport in Porous Media* **9**, 25–37.

Sorek, S., Bear, J., Ben-Dor, G. & Mazor, G. 1992 Shock waves in saturated thermoelastic porous media. *Transport in Porous Media* **9**, 3–13.

Zaretsky, E. & Ben-Dor, G. 1996 Thermodynamic law of corresponding shock states in flexible polymeric foams. *Trans. ASME: J. Engng Mat. Tech.* **118**, 493–502.